

Distribution of Liquid Mass in Transient Sprays Measured Using Laser-Plasma-Driven X-Ray Tomography

Diego Guénöt,¹ Kristoffer Svendsen,¹ Bastian Lehnert,^{2,3} Hannah Ulrich,^{3,4} Anders Persson,¹ Alexander Permogorov,¹ Lars Zigan,^{3,4} Michael Wensing,^{2,3} Olle Lundh,¹ and Edouard Berrocal^{1,3,5,*}

¹*Department of Physics, Division of Atomic Physics, Lund University, Sweden*

²*Lehrstuhl für Technische Thermodynamik, Friedrich-Alexander University Erlangen-Nürnberg, Germany*

³*Graduate School in Advanced Optical Technologies (SAOT), Friedrich-Alexander University Erlangen-Nürnberg, Germany*

⁴*Institut für Thermodynamik, Universität der Bundeswehr, München, Germany*

⁵*Division of Combustion Physics, Department of Physics, Lund University, Sweden*

(Received 6 November 2021; revised 25 March 2022; accepted 17 May 2022; published 28 June 2022)

We report the use of laser-plasma-driven x rays to reveal the three-dimensional (3D) structure of a highly atomizing water spray. Soft x rays approximately 5 keV are generated by means of a laser-plasma accelerator. Transmission radiography measurements are performed at different angles, by rotating a multihole injector. Using computer tomography, the local liquid volume distribution and its spatial variation are retrieved in 3D, showing up to 55% liquid fraction at the nozzle outlet, which decreases to below 7% within only 1 mm. The resolution of the liquid volume fraction is 0.5% while the spatial resolution of the radiographic images is 11.5 μm . The x-ray source used here provides successful measurements of liquid mass distribution over a relatively large volume and is very promising for the analysis of a variety of challenging transient spray systems, e.g., the injection of liquid synthetic and biofuels used for future clean-combustion applications.

DOI: 10.1103/PhysRevApplied.17.064056

I. INTRODUCTION

When a liquid jet is discharged at high injection pressure into a continuous gas, usually air, it is subjected to a series of liquid breakups that lead to the formation of irregular liquid bodies and, subsequently, to the formation of micrometric droplets that quickly evaporate. This process, known as atomization, is still not fully understood due to its complexity, its fast occurrence, and the lack of visibility imputed by multiple light-scattering effects. Atomizing sprays are particularly useful for the injection of liquid fuels, since the efficiency of a liquid-driven combustion device depends on the rapid liquid-to-gas transition of the injected fuel. Here, especially the primary breakup inside the nozzle due to cavitation and at the nozzle exit due to turbulence and aerodynamic effects is not fully understood. Controlling and optimizing this transition through a well-designed injection system allows reducing fuel consumption as well as pollutant emissions. Other relevant applications such as powder generation from spray drying, surface coating, flame spray pyrolysis, or spray cooling,

are all based on the use of specialized spray systems that need to be accurately characterized. Despite those needs, quantitative measurements as well as direct visualization of highly atomizing sprays are very challenging especially due to the occurrence and detection of multiple light scattering. Over the past two decades, several techniques have been developed to overcome those issues. The first approach consists in using visible light and rejecting the contribution from multiple scattering. The three main techniques capable of doing this are as follows:

(i) Ballistic imaging [1–3], where the late arrival photons reaching the detector and corresponding to the scattered light are temporally rejected by means of an ultra-short temporal Kerr gate.

(ii) Structured laser illumination planar imaging [4–6], where a spatially modulated light sheet is used and the nonmodulated component (corresponding to the intensity contribution from multiple light scattering) is being suppressed after image postprocessing.

(iii) Two-photon laser-induced fluorescence (2P LIF), where the scattered light does not have sufficient energy for generating fluorescence, allowing high-contrast images in comparison with single-photon excitation [7,8].

*edouard.berrocal@forbrf.lth.se

The second approach consists in using x rays. Unlike visible light, the refractive index of the injected liquid, such as water, approaches unity for photons in the keV range, resulting in negligible scattered radiation in comparison to the absorbed radiation. This makes the approach reliable for accurately measuring the liquid mass distribution near the nozzle, where large and irregular liquid bodies are still present and where the liquid density is the highest [9–12]. The attenuation length of soft x-rays depends on the liquid being injected and spans from 2 μm at 1 keV to 14 mm at 20 keV for water.

The liquid mass distribution is a helpful quantity for spray characterization as it is related to the rates of liquid breakups, gas entrainment, and evaporation over time. Measuring the local liquid volume fraction in the spray region, where droplets are already formed, can be achieved by means of a scanning structured light sheet [13]. The three-dimensional (3D) extinction coefficient has been obtained in 2012 using tomographic structured illumination [14], by rotating the injector, while instantaneous 3D reconstructions of a dilute hollow-cone spray have been achieved, the same year, using shadowgraphy images simultaneously recorded by four cameras [15].

Even if optical techniques based on structured illumination are capable of reconstructing the spray region in 3D at optical depth up to OD ~ 6 [16], the approach is limited when measuring the liquid volume fraction near the nozzle tip due to two main reasons: First, the Beer-Lambert law cannot be assumed in the spray formation region as the loss of light intensity along the incident direction is mostly due to refraction at the successive liquid-gas interfaces from large liquid bodies. Second, the remaining amount of unscattered photons is very low, usually resulting in a signal below the camera noise level.

This specific issue can be solved using soft x-ray absorption where the integrated liquid mass can successfully be measured near the nozzle where the spray is being formed [17]. X-ray tomography has been first used in 2003 [18] for two dimensions and in 2009 [19] for 3D reconstructions of a hollow-cone spray. The results have demonstrated noticeable asymmetries of liquid mass, leading to a nonuniform air-fuel mixing and a possible increase in NO_x or soot emission during combustion. Recently, hard x rays (50 keV) were used for tomographic reconstruction of cavitation inside a metallic nozzle [20]. To detect the liquid-gas interface after crossing 1–2 mm of steel, a phase-contrast configuration was used instead of direct absorption. To obtain the needed flux as well as the time resolution, the studies cited above have been performed at a large synchrotron facility, the Advanced Photon Source at Argonne National Laboratory. Some attempts in using other x-ray sources, such as medical computed tomography systems, have been limited to relatively low flux, long duration

of the x-ray pulse, and relatively low spatial resolution (e.g., 0.6 mm in Ref. [21]). Thus, the large majority of x-ray spray characterization originates from large synchrotron facilities making its accessibility limited. In addition, absorption measurements rely on using raster (point-by-point) scans [22,23], which are time consuming for two-dimensional (2D) reconstructions and highly challenging when considering 3D volumes in the range of 5–10 cm³.

In this paper, an alternative solution is employed, where x rays are generated by means of a laser-plasma accelerator, similarly to the work presented in Ref. [24]. In this scheme, an ultrashort laser pulse reaching intensities above 10¹⁸ W/cm² is used to ionize a gas medium, thus producing a plasma and exciting a plasma wave. If the focal spot size and pulse duration match the plasma wavelength, the plasma wave becomes highly nonlinear, and a cavity partially depleted of electrons forms behind the laser pulse [25]. In this cavity, there are strong focusing and accelerating electric fields (up to hundreds of GV/m) that can accelerate co-propagating electrons up to energies of hundreds of MeV and few mrad divergence over a few millimeters [26–28]. Several methods exist to inject electrons into this cavity for acceleration. In the present work, we use a gas mixture (helium and nitrogen) to inject electrons via the ionization injection mechanism proposed in Ref. [29]. It utilizes the fact that the innermost shells in nitrogen are ionized only at the intensity peak of the laser pulse to release electrons directly inside the cavity. During acceleration, the electrons oscillate transversely inside the plasma cavity; this motion leads to the generation of keV x rays in the forward direction [30].

A laser-plasma accelerator-based x-ray source has been developed over more than a decade at the Division of Atomic Physics, Lund University [31–33]. Previous studies have shown that laser-plasma-based x-ray sources are suitable for tomography [34], which is used in this study to obtain the 3D liquid mass distribution of a multihole gasoline direct-injection (GDI) spray. This multihole injector is designed for homogeneous combustion of improved gasoline used for engine applications. The operating conditions are equivalent to those presented in Ref. [7] where water is injected at 200-bar injection pressure and the spray is imaged at 200 μs after the visible start of injection. In this proof-of-concept paper, water is utilized as the working fluid instead of a combusting liquid fuel due to safety considerations at the test rig. First, the experimental setup is described followed by the 2D calibrated radiography. The results of the 3D tomography are given where horizontal sections at different heights from the nozzle tip are compared. Additionally, a comparison between the liquid volume fraction and planar two-photon LIF imaging is provided. Finally, the paper ends with a discussion on the potential use of the technique for future investigations of atomizing sprays involving the injection of liquid biofuels.

II. EXPERIMENTAL SETUP

The experimental setup is shown in Fig. 1. A laser pulse with an energy of 800 mJ and a pulse duration of 38 fs is focused to a spot size of 13 μm FWHM, reaching a peak intensity of 10^{19} W/cm^2 . At focus, the laser pulse enters a 6-mm-long gas cell containing a 99:1 gas mixture of He and N₂, resulting in an electron number density of 10^{19} cm^{-3} . An electron bunch (shown in blue) of several tens of pC is accelerated in the generated plasma up to a maximum energy of 200 MeV, with a final divergence of approximately 5-mrad FWHM [35]. The electron energy spectrum is measured by dispersing the electron bunch using a 0.8-T magnetic dipole onto a scintillating screen (Lanex), which is imaged using a 16-bit camera.

The x-ray pulses (in purple) are generated at a rate of 0.15 Hz in order to allow for the gas mixture to be pumped away and vacuum restored in the gas cell. Each pulse follows a synchrotronlike spectrum with a critical energy of 2.3 keV with a maximum energy of approximately 25 keV and a spectral peak located at 2 keV. The ultrashort pulse emanates from a source, which is less than 3 μm FWHM, containing approximately 10^{12} photons per steradian with a divergence of less than 30 mrad and pulse duration of a few fs [33,36,37].

The various filters (Al, Kapton, and Be windows) in the x-ray beam path absorbs the low-energy photons, prehardening the beam to have spectral peak at 5.5 keV. The spray is produced by a GDI Continental XL5 6-holes nozzle, with an orifice size of approximately 230 μm and intermittently separated jets, as shown in the microscopic image

of the nozzle plate and the radiography image as insets in Fig. 1.

The nozzle is operated at 200-bar liquid injection pressure using a high-pressure fuel-injection system. All the data presented here are recorded at 200 μs after the visible start of injection. The injected liquid is composed of water and 20% potassium iodide (KI) in order to increase x-ray absorption by a factor 2–3. Note that this mass concentration of KI changes the surface tension of the liquid by 2%, resulting in 74.2 mN/m, and the viscosity by 16%, resulting in 0.73 mm²/s, as detailed in the Supplemental Material from Ref. [24]. Note that these changes in the liquid properties are impacting the liquid breakups; means to avoid this is briefly discussed in the next section. The injector is mounted on a rotational system, motorized by a remotely controlled electronic stepper motor. This allows x-ray images of the spray at different angles to be recorded, while maintaining angular resolution under 0.1°. Images at angles from 0° to 180° are recorded by a step of 10°. To increase statistics and reduce noise level, images are averaged over 25 single shots at each angle. After crossing the spray, the x-ray pulse is detected using a 4-megapixel, 16-bit back-illuminated, deep-depletion x-ray camera with 13.5 μm pixel size (Andor iKon-L SO CCD). The pixel resolution of the recorded image is increased to 11.5 μm due to the magnification from the beam divergence.

III. X-RAY RADIOGRAPHY

A typical single-shot x-ray radiograph of the spray is shown in Fig. 2(a). Even if the main features of the spray

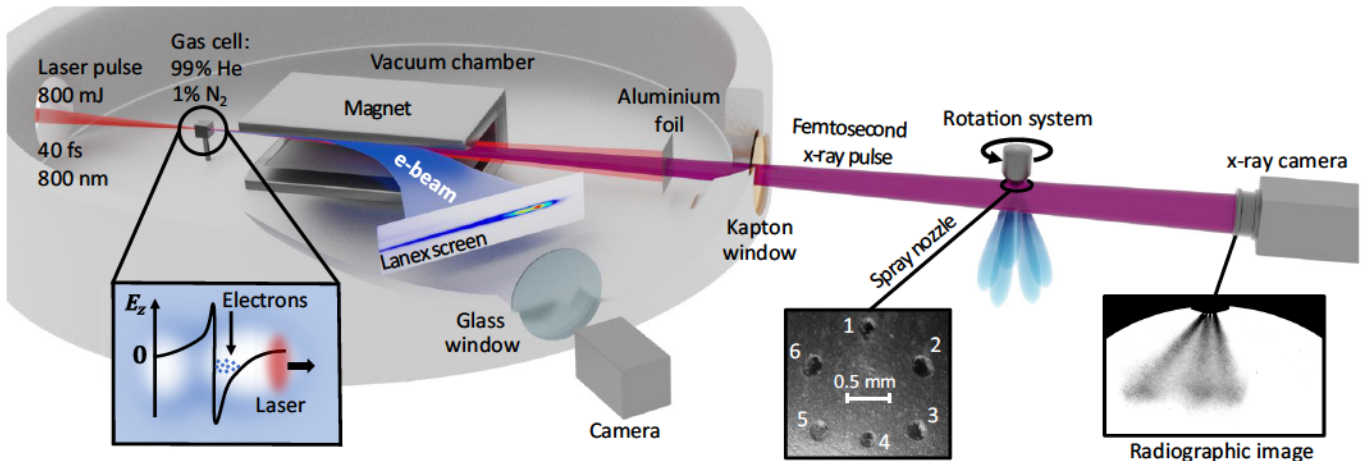


FIG. 1. Illustration of the experimental setup where femtosecond soft x-ray pulses are generated using a laser plasma accelerator (left). The incident intense laser pulse (red) propagates from left to right and generates the x-ray beam (purple) after being focused into a gas cell containing 99% helium and 1% nitrogen. The enlarged inset illustrates the laser plasma x-ray generation where the background plasma density is shown in light blue and white. The emitted electrons (blue) are deflected from the x-ray beam using a strong dipole magnet and imaged on a Lanex screen to obtain the electron-beam spectra. An aluminum foil and a Kapton vacuum window stops the laser radiation while allowing the x-ray beam to exit the vacuum chamber. The GDI spray nozzle is mounted on a motorized rotation stage. The enlarged inset shows a microscope image of the six holes of the injector each defined with a number. On the right, an averaged (25 single shots) x-ray image of the spray is provided.

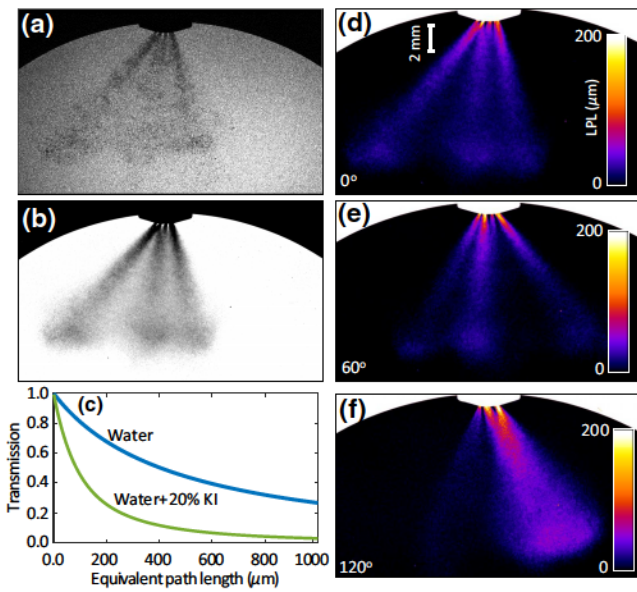


FIG. 2. Process for obtaining radiography images of the liquid path length. First, single-shot images (a) are recorded and an averaged image over 25 recordings is deduced (b). Then a calibration curve, shown in (c), is applied. The calibration curves shown in (c) correspond to the transmission of an x-ray beam with the same spectrum as measured at the detector as a function of equivalent path length for pure water and a mixture of water with 20% KI. Finally, the liquid path length is deduced, as exemplified for the rotation angle of 0° in (d), 60° in (e), and 120° in (f).

are visible, details are difficult to distinguish. By averaging over 25 exposures, as given in (b), the signal to noise level is greatly improved and each spray plume becomes clearly visible from the exit of the nozzle to its end, around 10 mm below. In order to account for the nonuniform background from the Gaussian-like x-ray beam-intensity distribution, a flat-field correction is applied on each image. The averaged images are then converted into a liquid path length (LPL) by means of a calibration curve, as shown in (c). The aim of the calibration is to convert x-ray intensity into a useful quantity for the tomography. It first requires to know the spectrum of the x-ray source. The x-ray spectrum generated by the laser-plasma accelerator is described by the following equation:

$$\frac{d^2I}{d\omega d\Omega} = N_b N_\beta \frac{3e^2}{2\pi^2 c} \gamma^2 \left(\frac{E}{E_c}\right)^2 \kappa_{2/3}^2 \left(\frac{E}{2E_c}\right),$$

with N_b the electron number, e the electric charge, c the speed of light, γ the Lorentz factor, $\kappa_{2/3}$ the modified Bessel function, E the photon energy, and E_c the critical energy. E_c is the only relevant parameter for the calibration since it determines the “shape” of the spectrum while the other parameters determine the total number of photons. The critical energy is measured using a Ross filter

array and $E_c = 2.3$ keV (± 0.3 keV) [24]. In order to obtain the spectrum at the detector, the effect of the 3- μm -thick aluminium foil, the 50- μm Kapton window, and 250- μm beryllium plate in front of the camera sensor, the 12 cm of air as well as the detector response function are considered. Finally, the absorption of any amount of liquid can be determined using the generalized Beer-Lambert law:

$$T(z) = \int_0^\infty e^{-\alpha(E)} S(E) dE,$$

where $S(E)$ is the normalized spectrum at the detector and $\alpha(E)$ is the absorption of the liquid [38]. The absorption for water and water +20% KI are shown in Fig. 2(c). Finally, we use the transmission $T(z)$ to convert the raw x-ray images into LPL. A flat-field correction is conducted to all the images in order to correct the effect of the x-ray beam-pointing fluctuation and nonflat intensity distribution.

The maximum liquid path length in Fig. 2 (d) is near 175 μm at the exit of the nozzles where no jets overlap and falls to 20 μm at the end of the spray 10 mm below the nozzle. Considering that the size of the orifices were around 230 μm this indicates that the liquid jets have already started to breakup when exiting the nozzle. Different orientations of the injector can be accurately adjusted as shown in Figs. 2(d)–2(f) corresponding to 0°, 60°, and 120° angles, respectively.

IV. X-RAY TOMOGRAPHY

The tomographic data is reconstructed from 475 calibrated projection images—from 475 independent injections—taken over 19 evenly spaced perspectives, ranging from 0° to 180°. For each perspective an image averaged over 25 single shots is generated, as shown in Fig. 2. To obtain the liquid volume fraction, see Figs. 3 and 4, the tomographic data is normalized to the voxel size.

A cubic spline interpolation is used to increase the number of projection angles from 19 to 179 in order to reduce streaking artifacts induced by the low number of projection angles [39]. The tomographic reconstruction is obtained by a filtered back-projection algorithm with a Ram-Lak filter in a parallel beam geometry. Due to the low x-ray beam divergence (approximately 10 mrad), the total root-mean-square error introduced by assuming a parallel beam geometry instead of a cone-beam geometry is found to be 0.7% by simulating a reconstruction of a Shepp-Logan phantom. A nonlocal median filter is applied to the tomographic data with a strength proportional to the nozzle distance to increase the signal-to-noise ratio far away from the nozzle, without compromising the spatial resolution close to the nozzle.

The resulting tomogram is rendered as 3D contour levels in Fig. 3(a). The liquid volume fraction ranges from 0.5%

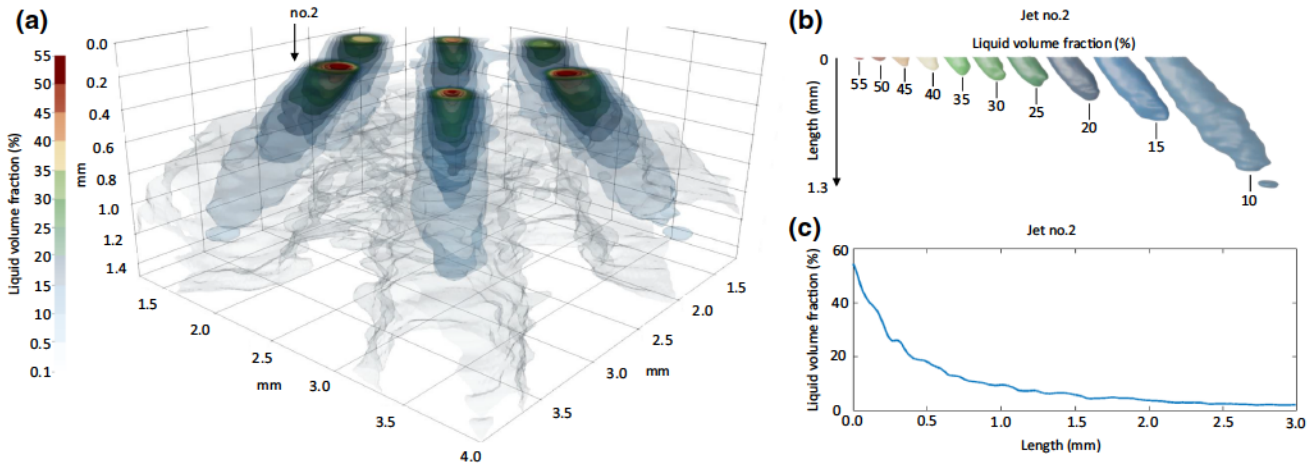


FIG. 3. (a) 3D tomographic reconstruction of the spray where the false colors indicate the liquid volume fraction in percent. (b) Contours for every 5% liquid volume fraction of jet no.2. (c) Line out of the liquid volume fraction along the center of jet no.2.

to 55%. The signal reaches the camera noise level below 0.5%. Thus, a threshold filter is applied at this value to remove the noise and increase visibility. The liquid volume fraction of the spray plume generated by orifice no.2 (indicated in Fig. 1), is extracted and shown in Fig. 3(b). Some isolated, local density distributions can be observed at the spray front, where the liquid volume fraction equals 10%. The liquid volume fraction rapidly reduces by a factor 10 over 1.5 mm as shown in Fig. 3(c) and approximately follows an exponential decay. This trend is further discussed in the subsequent paragraph.

Figures 4(a)–4(e) show horizontal slices at different heights from the nozzle tip; while (f)–(j) show vertical slices at different distances along the x axis. From those results, one can observe that the spray plumes are symmetrical along the vertical axis. Furthermore, not all spray plumes have the same size and shape due to the optimization of spray targeting and flow behavior in the respective holes. The maximum volume fraction at the exit of the spray is 55% and the liquid jet rapidly atomizes. It is known from the literature, that GDI jets—contrary to diesel primary jets—contain a high amount of gas (vapor and air), already at the nozzle exit due to cavitation and air entrainment. However, using optical techniques instead of x ray [40], the liquid volume fraction could not be quantified due to the aforementioned challenges.

The jets generated from the larger lateral orifices (no.2, 3, 5, and 6), have a steeper angle along the x direction [see (a)–(e)] in comparison with the jets generated by the smaller orifices, in the center (no.1 and 4). At 2 mm below the nozzle tip, shown in Fig. 4(e), it is observed that five spray plumes are merging together to form a single cloud of droplet while the plume no.1 still remains isolated. Additionally, it is observed that the smaller orifice diameters, corresponding to the holes no.1 and 4, result in a more prominent and compact spray core compared to the other,

larger orifices. Furthermore, the maximum LVF of spray plumes no.2 and 6 is found to be 40–50% higher than the spray plumes no.3 and 5, despite having identical orifice diameter.

Some minor artifacts can be observed in Fig. 4, which have an amplitude of about 4% of the maximum signal. This ratio remains similar when moving further down, away from the nozzle, making the artifacts more visible, see Fig. 4(j), and are therefore not an issue for interpreting the liquid mass distribution. The origin of these are likely due to the low number of projection angles and possibly minor beam-hardening artifacts. Although the beam hardening is taken into account in the analysis to a certain extent, the x-ray spectrum is assumed to have a specific shape and if the true shape deviates (in particular for low-energy x rays) this could lead to some minor beam-hardening artifacts.

To further improve the experimental setup, the low-energy x-ray transmission would need to be increased. This would allow for experiments without the need of KI additives and for the injection of other liquids. Achieving an x-ray spectrum with a lower critical energy would be advantageous for the same reason, as well as contributing to a higher signal-to-noise ratio, as the higher-energy x rays mainly contribute as noise in this application. Tailoring the electron injection mechanism in the plasma channel to produce a lower-energy x-ray spectrum could further improve the results. Another option would be to use a crystal monochromator to filter a specific x-ray energy, which would also prevent beam hardening with the downside of a reduction in x-ray flux. Due to the geometrical constraints of the vacuum chamber in the current setup, the distance between the x-ray source and the detector is 85 cm. However, decreasing this distance to 20 cm would increase the x-ray flux by a factor 25 while still covering the full spray area, greatly improving the signal-to-noise ratio.

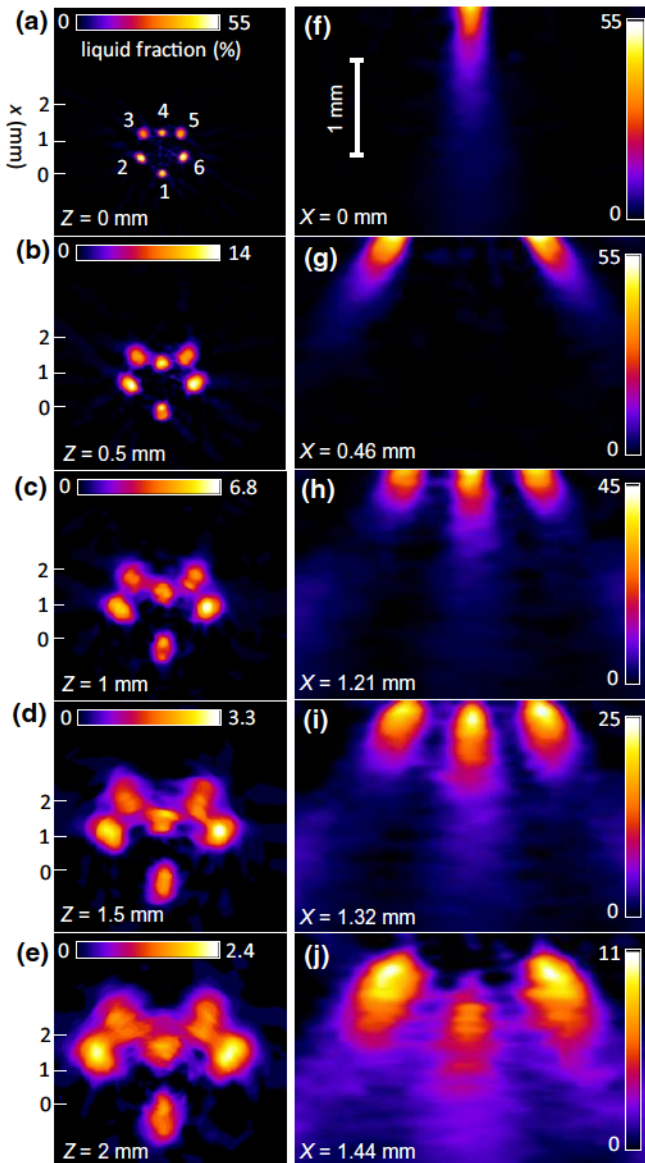


FIG. 4. Slice of the tomographic reconstruction showing the liquid volume fraction (in %) at different distances from the nozzle. Horizontal slices are shown on the left: (a) just at the exit of the nozzle (each jet is numbered), (b) at 500 μm below, (c) at 1 mm below, (d) at 1.5 mm below, and (e) at 2 mm below. Vertical slices are shown on the right: (f) along the center of the spray plume no.1, (g) the center of the spray plume no.2 and 6, (h)–(j) along the center of the spray plume no.3–5, respectively.

As mentioned in the introduction and demonstrated in Refs. [7,8], 2P LIF allows high-contrast single-shot visualization of atomizing sprays in the visible spectral range. By taking a portion of the femtosecond laser pulses used here, a light sheet approximately 30 μm in width, approximately 8-mJ pulse energy and 800-nm center wavelength is created for imaging the spray plume no.1. The corresponding experimental setup is illustrated in Fig. 5(a) and an example of the recorded 2P LIF single-shot image is shown in

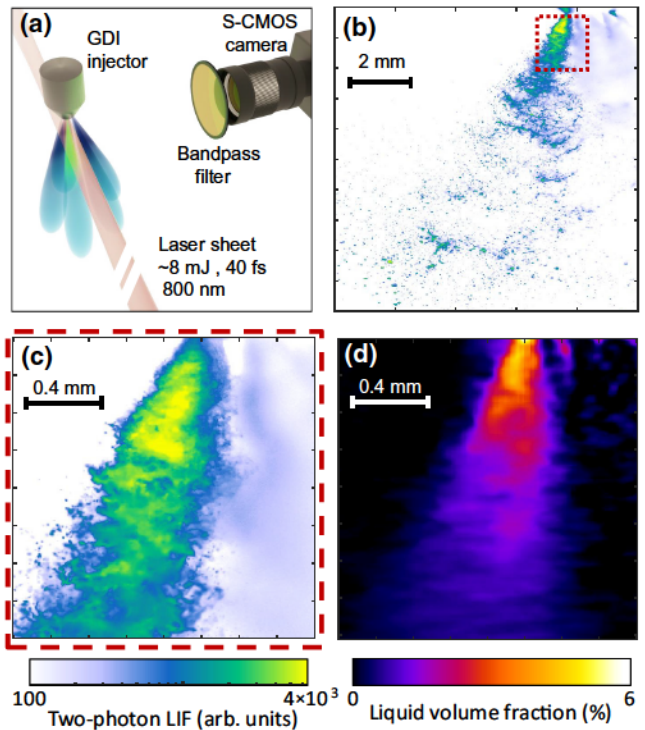


FIG. 5. (a) Experimental setup for 2P LIF imaging of the spray plume no.1. (b) Example of a resulting single-shot 2P LIF image where the laser sheet enters the spray at 70 μm away from the orifice center. (c) Enlarged view of the near nozzle region (red dashed box) while (d) is the corresponding 30 μm thickness vertical slice from the tomogram.

(b). The image is recorded with an sCMOS camera (Andor Zyla 5.5 Mpx) equipped with a 1 \times magnification telecentric lens objective resulting to 6.5 μm pixel resolution. A band-pass filter centered at 510 nm with 90 nm bandwidth is used to collect only the fluorescence signal. In the low-density spray region, a large number of individual droplets can be observed in Fig. 5(b). A dashed red box located near the orifice is magnified 5 \times in (c). This exact same area is deduced from the tomographic reconstruction and given in (d).

When comparing Figs. 5(c) and 5(d), a similar general shape of the spray is observed although a slightly different angle can be noticed. This is due to the fact that the 2P LIF detection is a single-shot image where the direction of injection and shape of the jet is fluctuating from one injection to another while the x-ray data is averaged. Thus, a one-to-one correspondence between the two is not to be expected. Of note, the two techniques provide different spray-related information:

For 2P LIF planar imaging, a qualitative description of the spray is obtained, where liquid structures can be visualized at high resolution from single-shot images. Additionally individual micrometric droplets located in the

low-density spray region [away from the nozzle tip, as seen in (b)] can still be resolved and imaged with a good contrast. Despite those benefits, it is very challenging, if not impossible, to relate the 2P LIF signal with the liquid volume fraction near the nozzle tip, due to the following: (1) Light refraction effects from large liquid bodies. (2) The occurrence of multiple light scattering by the surrounding micrometric droplets. (3) The nonlinear response of two-photon emission, which differs from one-photon LIF [41].

X rays, on the other hand, exhibit a negligible amount of refraction and scattering, which allows for quantitative measurements of the liquid volume fraction close to the nozzle tip, as shown in (d). However, far away from the nozzle, the absorption of the integrated liquid mass is approaching the absorption of air, resulting in a poor contrast. Thus, the two imaging techniques complement each other well, where x-ray imaging provides quantitative imaging through high liquid density regions (near the nozzle tip) while 2P LIF imaging reveals liquid elements within regions of lower liquid density .

V. CONCLUSION

In this paper, we show that soft x-ray beams produced by a laser-plasma accelerator are well suited for tomographic reconstructions of advanced spray systems, where both high spatial resolution and large imaging area is needed. Additionally, the high x-ray flux combined with the ultra-short nature of the x-ray pulse makes the source suitable for the study of highly transient two-phase flows. Furthermore, the tomogram reaches a liquid volume fraction resolution of 0.5%, while the pixel resolution of the radiography images is $11.5 \mu\text{m}$. The liquid volume fraction at the nozzle exit is found to be in the range of 55%, which confirms assumptions in the literature. This is an essential finding as no quantitative data on volume fraction near the nozzle tip exists so far for the development and validation of spray atomization models.

To conclude, this work is an essential step towards future measurements of the 3D evolution of the liquid mass over its injection cycle, by repeating it at different times after the start of injection. Its capability for generating radiography images with a large field of view is very advantageous for the 3D reconstruction of large spray volumes. In addition, the technique can easily be combined with 2P LIF imaging at no extra costs, providing valuable additional spray information such as droplet size. Future findings from such measurements can lead to a deeper understanding on the formation and behavior of highly atomizing sprays, especially for alternative synthetic and biogenic fuels. This may show the influence of different fluid properties on the atomization quality.

ACKNOWLEDGMENTS

This project has received funding from the European Union's Horizon 2020 Research and Innovation programme under Grant Agreement No. 730871 (ARIES), the European Research Council (ERC) Starting Grant: "Spray-Imaging"—638546, the Swedish Research Council (2016-03894 and 2019-04784), the Knut and Alice Wallenberg Foundation (KAW 2019.0318) and the Erlangen Graduate School in Advanced Optical Technologies (SAOT), which is funded by the federal state of Bavaria. The authors D.G. and K.S. contributed equally to this work.

- [1] M. Paciaroni and M. Linne, Single-shot, two-dimensional ballistic imaging through scattering media, *Appl. Opt.* **43**, 5100 (2004).
- [2] M. A. Linne, M. Paciaroni, E. Berrocal, and D. Sedarsky, Ballistic imaging of liquid breakup processes in dense sprays, *Proc. Combust. Inst.* **32**, 2147 (2009).
- [3] H. Purwar, S. Idlahcen, C. Rozé, D. Sedarsky, and J.-B. Blaisot, Collinear, two-color optical kerr effect shutter for ultrafast time-resolved imaging, *Opt. Express* **22**, 15778 (2014).
- [4] E. Berrocal, E. Kristensson, M. Richter, M. Linne, and M. Aldén, Application of structured illumination for multiple scattering suppression in planar laser imaging of dense sprays, *Opt. Express* **16**, 17870 (2008).
- [5] Y. N. Mishra, E. Kristensson, M. Koegl, J. Jönsson, L. Zigan, and E. Berrocal, Comparison between two-phase and one-phase SLIPI for instantaneous imaging of transient sprays, *Exp. Fluids* **58**, 110 (2017).
- [6] E. Kristensson and E. Berrocal, Crossed patterned structured illumination for the analysis and velocimetry of transient turbid media, *Sci. Rep.* **8**, 11751 (2018).
- [7] E. Berrocal, J. P. C. Conrad, C. L. Arnold, M. Wensing, M. Linne, and M. Miranda, Two-photon fluorescence laser sheet imaging for high contrast visualization of atomizing sprays, *OSA Contin.* **2**, 983 (2019).
- [8] H. Ulrich, B. Lehnert, D. Guénöt, K. Svendsen, O. Lundh, S. Will, M. Wensing, E. Berrocal, and L. Zigan, in *15th International Conference on Liquid Atomization and Spray System*, ICLASS (Edinburgh, Scotland, 2021).
- [9] C. F. Powell, Y. Y. R. Poola, and J. Wang, Time-resolved measurements of supersonic fuel sprays using synchrotron x-rays, *J. Synchrotron Radiat.* **7**, 356 (2000).
- [10] A. G. MacPhee, M. W. Tate, C. F. Powell, Y. Y. M. J. Renzi, A. Ercan, S. Narayanan, E. Fontes, J. Walther, J. Schaller, S. M. Gruner, X-ray imaging of shock waves generated by high-pressure fuel sprays, *Science* **295**, 1261 (2002).
- [11] C. F. Powell, S. A. Ciatti, S.-K. C. J. Liu, and J. Wang, X-ray absorption measurements of diesel sprays and the effects of nozzle geometry, *SAE Tech. Pap.*, 2004 (2004).
- [12] B. R. Halls, C. D. Radke, B. J. Reuter, A. L. Kastengren, J. R. Gord, and T. R. Meyer, High-speed, two-dimensional synchrotron white-beam x-ray radiography of spray breakup and atomization, *Opt. Express* **25**, 1605 (2017).

- [13] Y. N. Mishra, T. Tscharntke, E. Kristensson, and E. Berrocal, Application of SLIP-based techniques for droplet size, concentration, and liquid volume fraction mapping in sprays, *Appl. Sci.* **10**, 1369 (2020).
- [14] E. Kristensson, E. Berrocal, and M. Aldén, Quantitative 3D imaging of scattering media using structured illumination and computed tomography, *Opt. Express* **20**, 14437 (2012).
- [15] J. Klinner and C. Willert, Tomographic shadowgraphy for three-dimensional reconstruction of instantaneous spray distributions, *Exp. Fluids* **53**, 531 (2012).
- [16] H. Grosshans, E. Kristensson, R.-Z. Szász, and E. Berrocal, Prediction and measurement of the local extinction coefficient in sprays for 3D simulation/experiment data comparison, *Int. J. Multiphase Flow* **72**, 218 (2015).
- [17] M. Linne, Analysis of x-ray radiography in atomizing sprays, *Exp. Fluids* **53**, 655 (2012).
- [18] W. Cai, C. F. Powell, S. N. Y. Yue, J. Wang, M. W. Tate, M. J. Renzi, A. Ercan, E. Fontes, and S. M. Gruner, Quantitative analysis of highly transient fuel sprays by time-resolved x-radiography, *Appl. Phys.* **83**, 1671 (2003).
- [19] X. Liu, K.-S. Im, Y. Wang, J. Wang, M. W. Tate, A. Ercan, D. R. Schuette, and S. M. Gruner, Four dimensional visualization of highly transient fuel sprays by microsecond quantitative x-ray tomography, *Appl. Phys.* **94**, 084101 (2009).
- [20] A. Tekawade, B. A. Sforzo, K. E. Matusik, K. Fezzaa, A. L. Kastengren, and C. F. Powell, Time-resolved 3D imaging of two-phase fluid flow inside a steel fuel injector using synchrotron x-ray tomography, *Sci. Rep.* **10**, 8674 (2020).
- [21] F. Coletti, M. J. Benson, A. L. Sagues, B. H. Miller, R. Fahrig, and J. K. Eaton, Three-dimensional mass fraction distribution of a spray measured by x-ray computed tomography, *J. Eng. Gas. Turbine Power* **136**, 051508 (2014).
- [22] B. A. Sforzo, A. Tekawade, K. E. Matusik, A. L. Kastengren, J. Ilavsky, and C. F. Powell, in *29th European Conference on Liquid Atomization and Spray System*, ILASS-Europe (Paris, France, 2019).
- [23] D. J. Duke, A. B. Swantek, N. M. Sovis, F. Z. Tilocco, C. F. Powell, D. G. A. L. Kastengren, and T. Biçer, Time-resolved x-ray tomography of gasoline direct injection sprays, *SAE Int. J. Engines* **9**, 143 (2016).
- [24] D. Guénot, K. Svendsen, J. B. Svensson, H. Ekerfelt, O. L. A. Persson, and E. Berrocal, Simultaneous laser-driven x-ray and two-photon fluorescence imaging of atomizing sprays, *Optica* **7**, 131 (2020).
- [25] W. Lu, M. Tzoufras, C. Joshi, F. S. Tsung, W. B. Mori, J. Vieira, R. A. Fonseca, and L. O. Silva, Generating multi-GeV electron bunches using single stage laser wakefield acceleration in a 3D nonlinear regime, *Phys. Rev. ST Accel. Beams* **10**, 061301 (2007).
- [26] J. Faure, Y. Glinec, A. Pukhov, S. Kiselev, S. Gordienko, E. Lefebvre, J.-P. Rousseau, F. Burgay, and V. Malka, A laser-plasma accelerator producing monoenergetic electron beams, *Nature* **431**, 541 (2004).
- [27] C. G. R. Geddes, C. Tóth, J. van Tilborg, E. Esarey, C. B. Schroeder, D. Bruhwiler, C. Nieter, J. Cary, and W. P. Leemans, High quality electron beams from a laser wakefield accelerator using plasma-channel guiding, *Nature* **431**, 538 (2004).
- [28] S. Mangels, C. D. Murphy, Z. Najmudin, A. G. R. Thomas, J. L. Collier, A. E. Dangor, A. J. Divall, P. S. Foster, J. G. Gallacher, C. J. Hooker, D. A. Jaroszynski, A. J. Langley, W. B. Mori, P. A. Norreys, F. S. Tsung, R. Viskup, B. R. Walton, and K. Krushelnick, Mono-energetic beams of relativistic electrons from intense laser plasma interactions, *Nature* **431**, 535 (2004).
- [29] A. Pak, K. A. Marsh, S. F. Martins, W. Lu, W. B. Mori, and C. Joshi, Injection and Trapping of Tunnel-Ionized Electrons into Laser-Produced Wakes, *Phys. Rev. Lett.* **104**, 025003 (2010).
- [30] A. Rousse, K. T. Phuoc, R. Shah, A. Pukhov, E. Lefebvre, V. Malka, S. Kiselev, F. Burgay, J. Rousseau, D. Umstadter, *et al.*, Production of a keV X-ray Beam from Synchrotron Radiation in Relativistic Laser-Plasma Interaction, *Phys. Rev. Lett.* **93**, 135005 (2004).
- [31] S. Mangels, G. Genoud, S. Kneip, M. Burza, K. Cassou, B. Cros, N. Dover, C. Kamperidis, Z. Najmudin, A. Persson, *et al.*, Controlling the spectrum of x-rays generated in a laser-plasma accelerator by tailoring the laser wavefront, *Appl. Phys.* **95**, 18116 (2009).
- [32] J. Ju, K. Svensson, A. Döpp, H. Ferrari, K. Cassou, O. Neveu, G. Genoud, F. Wojda, M. Burza, A. Persson, *et al.*, Enhancement of x-rays generated by a guided laser wakefield accelerator inside capillary tubes, *Appl. Phys. Lett.* **100**, 191106 (2012).
- [33] K. Svendsen, I. G. González, M. Hansson, J. B. Svensson, H. Ekerfelt, A. Persson, and O. Lundh, Optimization of soft x-ray phase-contrast tomography using a laser wakefield accelerator, *Opt. Express* **26**, 33930 (2018).
- [34] J. M. Cole, *et al.*, High-resolution μ CT of a mouse embryo using a compact laser-driven x-ray betatron source, *Proc. Natl. Acad. Sci.* **115**, 6335 (2018).
- [35] I. G. González, H. Ekerfelt, M. Hansson, T. Audet, B. Aurand, F. Desforges, S. D. Dufrénoy, A. Persson, X. Davoine, and C. Wahlström, Effects of the dopant concentration in laser wakefield and direct laser acceleration of electrons, *New J. Phys.* **20**, 053011 (2018).
- [36] S. Corde, K. T. Phuoc, A. Beck, G. Lambert, R. Fitour, E. Lefebvre, V. Malka, and A. Rousse, Femtosecond X rays from laser-plasma accelerators, *Rev. Mod. Phys.* **85**, 1 (2013).
- [37] F. Albert and A. G. R. Thomas, Applications of laser wakefield accelerator-based light sources, *Plasma Phys. Controlled Fusion* **58**, 103001 (2016).
- [38] X-ray interactions with matter, http://henke.lbl.gov/optical_constants/.
- [39] E. Enjilela, T. Y. Lee, G. Wisenberg, P. Teefy, R. Bagur, A. Islam, J. Hsieh, and A. So, Cubic-spline interpolation for sparse-view CT image reconstruction with filtered backprojection in dynamic myocardial perfusion imaging, *Tomography* **5**, 300 (2019).
- [40] A. Durst, M. Wensing, and E. Berrocal, Light sheet fluorescence microscopic imaging for the primary breakup of diesel and gasoline sprays with real-world fuels, *Appl. Opt.* **57**, 2704 (2018).
- [41] A. Roth, D. Frantz, W. Chaze, A. Corber, and E. Berrocal, High-speed imaging database of water jet disintegration part I: Quantitative imaging using liquid laser-induced fluorescence, *Int. J. Multiphase Flow* **145**, 103641 (2021).